



# Synthesis of bilayer borophene

Caiyun Chen<sup>1,2,5</sup>, Haifeng Lv<sup>3,5</sup>, Ping Zhang<sup>1,2</sup>, Zhiwen Zhuo<sup>3</sup>, Yu Wang<sup>1,2</sup>, Chen Ma<sup>1,2</sup>, Wenbin Li<sup>1,2</sup>, Xuguang Wang<sup>1,2</sup>, Baojie Feng<sup>1,2</sup>, Peng Cheng<sup>1,2</sup>, Xiaojun Wu<sup>3</sup>✉, Kehui Wu<sup>1,2,4</sup>✉ and Lan Chen<sup>1,2,4</sup>✉

**As the nearest-neighbour element to carbon, boron is theoretically predicted to have a planar two-dimensional form, named borophene, with novel properties, such as Dirac fermions and superconductivity. Several polymorphs of monolayer borophene have been grown on metal surfaces, yet thicker bilayer and few-layer nanosheets remain elusive. Here we report the synthesis of large-size, single-crystalline bilayer borophene on the Cu(111) surface by molecular beam epitaxy. Combining scanning tunnelling microscopy and first-principles calculations, we show that bilayer borophene consists of two stacked monolayers that are held together by covalent interlayer boron–boron bonding, and each monolayer has  $\beta_{12}$ -like structures with zigzag rows. The formation of a bilayer is associated with a large transfer and redistribution of charge in the first boron layer on Cu(111), which provides additional electrons for the bonding of additional boron atoms, enabling the growth of the second layer. The bilayer borophene is shown to possess metallic character, and be less prone to being oxidized than its monolayer counterparts.**

The rise of graphene has motivated great interest on the science and applications of elemental two-dimensional (2D) materials<sup>1–4</sup>. As the neighbouring element of carbon in the periodic table, boron has a strong bonding capability, comparable to that of carbon. Extensive studies on small planar boron clusters, especially B<sub>36</sub>, provided the first experimental evidence for the viability of 2D boron, named borophene<sup>5–7</sup>. The discovery of borophene enriched the physics and chemistry of boron<sup>8–16</sup>. The novel properties of borophene, such as mechanical compliance<sup>17,18</sup>, optical transparency<sup>19</sup>, anisotropic plasmonics<sup>20,21</sup>, ultrahigh thermal conductance<sup>22,23</sup>, 1D nearly-free-electron state<sup>24</sup>, the presence of metallic Dirac fermions<sup>25,26</sup> and superconductivity<sup>27–29</sup>, have attracted intensive theoretical and experimental interest. To date, several monolayer borophene polymorphs with different atomic structures have been synthesized by molecular beam epitaxy (MBE) on a variety of metal surfaces, which include Ag(111)/(110)/(100)<sup>14,15,30–33</sup>, Al(111)<sup>34</sup>, Au(111)<sup>35</sup>, Cu(111)<sup>36,37</sup> and Ir(111)<sup>38</sup>. In these studies, metal surfaces served as 2D templates that stabilized the formation of 2D boron. Besides that, the production of free-standing 2D boron sheets by liquid-phase exfoliation has also been reported, in which thin boron flakes are peeled from the boron bulk by ultrasonic energy<sup>39–41</sup>.

Recently, increasing interest has been drawn to few-layer 2D materials, such as twisting bilayer graphene<sup>42,43</sup> and few-layer transition metal dichalcogenides and their heterojunctions<sup>44–48</sup>, because these structures exhibit more intriguing properties as well as tunability than their monolayer counterparts. This is also expected to be the case for 2D boron. Bilayer borophene was predicted to be more stable than the monolayer borophene due to the bonding between the two layers<sup>49–51</sup>, and is a candidate material for a wide range of applications, which range from nodal-line semimetals<sup>50,52</sup> to superconductors<sup>53</sup> and anodes in lithium-ion batteries<sup>54</sup>. However, bilayer or few-layer borophene has not been synthesized so far. Experimentally, once monolayer borophene forms on metal substrates, such as Ag(111), the deposition of more boron atoms

typically results in the formation of 3D clusters instead of a flat multilayer boron structure<sup>14,15</sup>. It is not yet known whether a 2D boron structure is self-sustainable or has to be maintained by interaction with a substrate. Additionally, a recent work on the structural diversity of boron nanoclusters found that the bilayer B<sub>48</sub><sup>−/0</sup> clusters are much more stable than other isomers due to the interlayer bonding, which provides a clue to the possibility of realizing bilayer borophene<sup>55</sup>.

Here we describe the synthesis of uniform, large-size (up to millimetres) bilayer borophene on the Cu(111) surface by MBE. Through a combination of scanning tunnelling microscopy (STM) and density functional theory (DFT) calculations, the structure of the bilayer borophene was shown to be two boron sheets stacked to each other through covalent interlayer boron–boron bonding; each sheet has a  $\beta_{12}$ -like structure with zigzag boron rows, in a similar manner to the  $\beta_{12}$  monolayer grown on an Ag(111) surface. This bilayer borophene was found to be more stable than the free-standing monolayer. The high adsorption energy of the first boron layer on Cu(111) and the redistribution of the charge in this layer were found to favour the formation of a second boron layer. It is worth noting that during the publication of this work, a parallel work on the synthesis of bilayer borophene on an Ag(111) substrate was reported by Liu et al.<sup>56</sup>

## Growth and STM characterizations

Boron atoms were evaporated by an electron-beam evaporator on to the Cu(111) surface at various substrate temperatures ( $T_s$ ). For  $T_s$  below 500 K, only clusters and disordered structures were formed on the surface. As  $T_s$  was increased to above 600 K, a long-range ordered structure appeared that expanded to cover the entire surface with an increasing boron coverage (Fig. 1a). The unit cell of the ordered structure is marked in the high-resolution STM images shown in Fig. 2a,b and its lattice constants are:  $a_1 \approx 16.0 \text{ \AA}$ ,  $b_1 \approx 21.6 \text{ \AA}$  and  $\theta_1 \approx 70^\circ$ . This unit cell can be described as  $\sqrt{73} \times \sqrt{39}$  with

<sup>1</sup>Institute of Physics, Chinese Academy of Sciences, Beijing, China. <sup>2</sup>School of Physical Sciences, University of Chinese Academy of Sciences, Beijing, China.

<sup>3</sup>Hefei National Laboratory for Physical Sciences at the Microscale, Synergetic Innovation of Quantum Information and Quantum Technology, CAS Center for Excellence in Nanoscience, and School of Chemistry and Materials Sciences, University of Science and Technology of China, Hefei, China. <sup>4</sup>Songshan Lake Materials Laboratory, Dongguan, China. <sup>5</sup>These authors contributed equally: Caiyun Chen, Haifeng Lv. ✉e-mail: [xjwu@ustc.edu.cn](mailto:xjwu@ustc.edu.cn); [khwu@iphy.ac.cn](mailto:khwu@iphy.ac.cn);

[lchen@iphy.ac.cn](mailto:lchen@iphy.ac.cn)

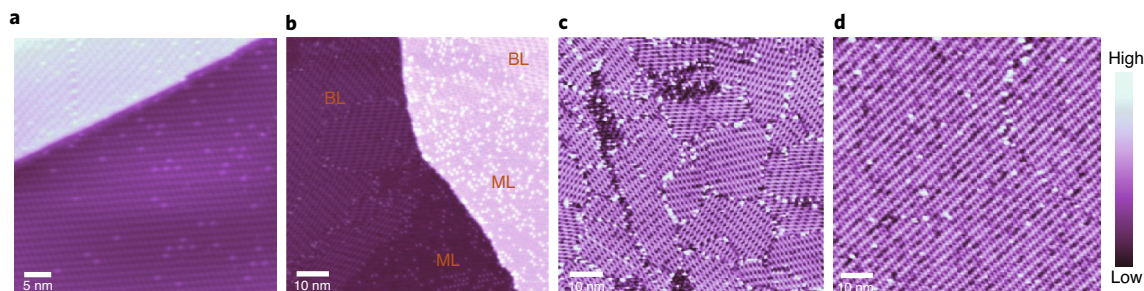


**Fig. 1 | STM images showing the evolution of the Cu(111) surface with increasing B coverage.** **a**, Monolayer borophene on Cu(111) ( $I=90$  pA,  $V=1.2$  V). **b**, Coexisting monolayer (ML) and bilayer (BL) borophene ( $I=80$  pA,  $V=-1.0$  V). The dark and bright areas in **a** and **b** represent the borophene on different terraces of the Cu(111) surface. **c**, A Cu(111) surface fully covered by bilayer borophene ( $I=90$  pA,  $V=0.95$  V). **d**, Bilayer borophene with a large single-phase domain, obtained after annealing the surface in **c** at 750 K ( $I=90$  pA,  $V=-1.5$  V). The colour scale refers to different heights in **a-d**.

respect to the  $1\times 1$  lattice of Cu(111). This result is in agreement with the previous report by Wu et al. who identified this structure as a monolayer boron sheet on Cu(111)<sup>36</sup>.

It is noteworthy that after the entire Cu(111) surface was covered by monolayer borophene, a new ordered structure appeared when more boron atoms were evaporated onto the surface, as shown in Fig. 1b. With the increase of the boron coverage to approximately twice the coverage of monolayer borophene, this new phase extended to cover the entire surface, as shown in Fig. 1c. The new structure was higher than monolayer borophene in STM images taken at all biases (Supplementary Fig. 4). The coverage calibration and the height feature indicate that this new structure corresponds to bilayer borophene. Notably, the bilayer borophene domains exhibited six different orientations, which correspond to three equivalent directions related to each other by  $120^\circ$  rotations and their mirror-symmetric counterparts. After annealing the sample at a higher substrate temperature ( $\sim 750$  K), a surface with a uniform and large, single-phase domain was formed, as shown in Fig. 1d. The high-resolution STM image of bilayer borophene before and after annealing showed the same structure (Fig. 2d). The quality of bilayer borophene was also reflected by the good continuity of the film across the steps of the substrate (Supplementary Fig. 6).

Figure 2d,e shows high-resolution STM images of two bilayer borophene domains with mirror-symmetric orientations, from which one can obtain the lattice constants of the unit cell:  $a_2 \approx 16.2$  Å,  $b_2 \approx 33$  Å and  $\theta_2 \approx 69^\circ$ . The image of the bilayer borophene consists of parallel chains, with alternative bright and dark protrusions that have an elongated ellipsoid shape. The distance between the nearest-neighbour protrusions was about 5 Å along the chains. Another readily noticeable feature is that the directions of the ellipsoid protrusions in the neighbour chains are rotated by  $120^\circ$  in a zigzag-like manner. Notably, we found that after the formation of the bilayer borophene on the entire Cu(111) surface, the further deposition of boron atoms resulted in 3D boron clusters instead of thicker borophene layers (Supplementary Fig. 2). Thus, the growth of 2D boron on Cu(111) is terminated by the formation of bilayer borophene on Cu(111), which is different from the case of boron on the Ag(111) surface. In latter case, the growth of 2D boron on Ag(111) is terminated by the formation of monolayer borophene<sup>14,15</sup>.

### Models and calculations

To understand the mechanism for the formation of bilayer borophene, the detailed atomic structure of bilayer borophene must be worked out initially. We first compared the unit cell of bilayer borophene with that of monolayer borophene (with lattice vectors  $\mathbf{a}_1$  and  $\mathbf{b}_1$ ). The direction of the lattice vector  $\mathbf{a}_2$  of the bilayer borophene is parallel to  $\mathbf{a}_1$ , and there is a small rotation angle ( $\sim 1^\circ$ ) between the directions of  $\mathbf{b}_2$  and  $\mathbf{b}_1$ . Therefore, the unit cell of bilayer

corresponds to a  $\sqrt{178} \times \sqrt{39}$  superstructure that is rotated by a small angle ( $\sim 7^\circ$ ) with respect to the  $[1\bar{1}0]$  direction of the Cu(111) surface (for the monolayer, the angle is  $\sim 5.8^\circ$ ). We performed an extensive search for possible structural models for bilayer borophene on the Cu(111) surface, and an exceptionally stable model was found based on the analysis of first-principles calculations and STM images, as shown in Fig. 2g. This model consists of two flat boron sheets with a similar atomic structure (as shown in Fig. 2h,i). Each boron sheet has a  $\beta_{12}$ -like structure with a periodic zigzag-type modulation. The optimized lattice constants of the unit cell are  $a=16.1$  Å,  $b=34.2$  Å and  $\theta=69.2^\circ$ , in agreement with the experimental values. The lattice mismatch between the bilayer borophene and Cu substrate is smaller than 0.3%. To better characterize borophene structures, the hexagonal hole (HH) density, defined as  $\eta = \text{number of HHs}/\text{number of atoms in a triangular lattice}$ , is often used. In our case, the first (bottom) layer of bilayer borophene includes 186 boron atoms per cell, with a HH density of  $\eta=5/36$  (Fig. 2h). The second (top) layer has similar atomic structure, but with six missing boron atoms, resulting in HH density of  $\eta=1/6$  (Fig. 2i), identical to that of the  $\beta_{12}$  structure<sup>15,31</sup>. The total HH density of bilayer borophene is  $11/72$ , slightly lower than that of the  $\beta_{12}$  phase ( $1/6$ ) on the Ag(111) surface<sup>15,31</sup>.

In the bilayer model, the second layer slides by approximately 1.72 Å from the first layer in the in-plane direction, and the interlayer distance is 1.82 Å, which indicates the formation of covalent interlayer bonds between the four-coordinated boron atoms (shown in yellow in Fig. 2h,i). The stacking of two boron layers with slightly different unit cells induces a periodic modulation of the density of states (DOS)<sup>57</sup>, which accounts for the different brightness of protrusions in STM image (Fig. 2d,e). The simulated STM image (Fig. 2f) is in good agreement with the experimental results, and includes the ellipsoid shape of the protrusions, zigzag-like arrangement and alternating bright and dark sections along the chains. The experimentally calibrated atomic densities of monolayer and bilayer borophene were  $35.87 \pm 0.43$  nm<sup>-2</sup> and  $71.74 \pm 0.86$  nm<sup>-2</sup>, respectively (see details of the boron coverage calibration in Supplementary Information), which accord with the values from theoretical models ( $\sim 36.14$  nm<sup>-2</sup> and  $71.1$  nm<sup>-2</sup>, respectively) very well and support the validity of our model.

The validity of this bilayer structural model is supported by its large energy stability. We compared the formation energy ( $E$  (eV atom<sup>-1</sup>)) of the free-standing bilayer borophene and the well-known  $\beta_{12}$  monolayer borophene (the structure model and lattice parameters are shown in Supplementary Fig. 10 and Supplementary Table 1), as summarized in Table 1. It was found that the energy of bilayer borophene was 55 meV atom<sup>-1</sup> lower than the energy of the  $\beta_{12}$  monolayer borophene, which implies it has a higher thermal stability. The high thermal stability of bilayer borophene

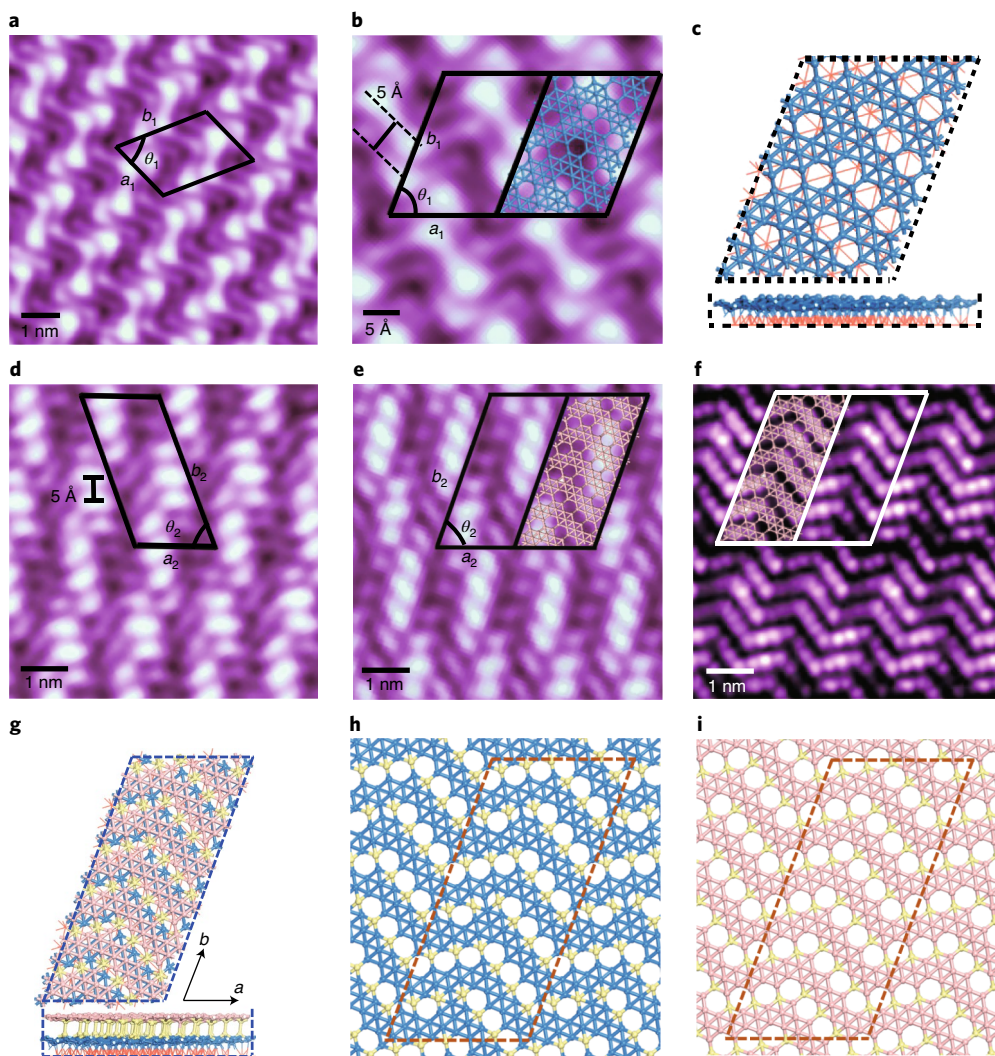


**Fig. 2 | High-resolution STM images and structural models of monolayer and bilayer borophene on Cu(111).** **a**, High-resolution images of monolayer borophene on a Cu surface ( $I=210$  pA,  $V=-0.1$  V). The unit cell is marked by a black parallelogram. **b**, The zoomed-in STM image is also overlaid with a structural model (blue) ( $I=95$  pA,  $V=0.3$  V). **c**, A structural model of monolayer borophene. The blue spheres represent the first-layer boron atoms, and the underlying substrate, Cu(111), is shown in orange. **d,e**, High-resolution STM images of bilayer borophene with mirror symmetric orientations on the Cu(111) surface ( $I=90$  pA,  $V=0.5$  V). The two unit cells, one in **d** and its mirror-symmetric counterpart in **e**, are marked by black parallelograms. The pink spheres represent the second-layer boron atoms. **f**, Simulated STM image based on the bilayer structural model shown in **g**. The models of the boron sheets are superimposed on both the experimental (**e**) and simulated (**f**) STM images, and show very good agreement with the experimental results. **g**, Top view (top) and side view (bottom) of the calculated atomic structure of bilayer borophene. **h,i**, The detailed atomic structures of the first (**h**) and second (**i**) layers of bilayer borophene from the top view, in which the yellow spheres represent the boron atoms that form interlayer boron–boron bonds.

stems from the formation of interlayer covalent bonds between the four-coordinated boron atoms in the second and first boron layers. In fact, we calculated the energies of the first and second boron layers without interlayer bonding, and found that these would  $33$  meV  $\text{atom}^{-1}$  lower and  $6$  meV  $\text{atom}^{-1}$  higher, respectively, than that of the free-standing  $\beta_{12}$  monolayer, which implies that the formation of interlayer boron–boron covalent bonding plays a key role in stabilizing the 2D bilayer structure. Additionally, a Bader charge analysis revealed that the formation of interlayer covalent bonds results in a local charge redistribution around the interlayer-bonded boron atoms (Supplementary Fig. 15) and induces the wrinkled structure of bilayer borophene. In addition, the stability of bilayer boron can be further confirmed by our normal mode analysis as well as by the *ab initio* molecular dynamics simulation of bilayer boron (details in Supplementary Information). The bilayer boron sheet can be stable at  $1,000$  K without structural collapse or decomposition, and the interlayer boron bonds are well-preserved.

### Discussion of growth mechanism

The above model provides us with insight as to the formation mechanism of bilayer borophene on Cu(111). It is known that the interactions between a metal substrate and boron are crucial for the formation of 2D boron<sup>11–15,30–38</sup>. The adsorption energy of the first boron layer on the Cu(111) substrate is  $-0.41$  eV  $\text{atom}^{-1}$  ( $-0.148$  eV  $\text{\AA}^{-2}$ ), which is approximately twice that of the  $\beta_{12}$  monolayer on the Ag(111) substrate ( $-0.22$  eV  $\text{atom}^{-1}$  or  $-0.074$  eV  $\text{\AA}^{-2}$ ), as summarized in Table 2. Bader charge analysis indicates that approximately  $0.026$  e is transferred to each boron atom, which is much larger than the charge transfer on the Ag(111) substrate<sup>15</sup> (approximately  $0.014$  e per boron atom). The relatively large electron transfer to the first boron layer provides additional electron density for bonding with the boron atoms in the second layer, which enables its growth. The differential charge density distribution also shows electron accumulation in bilayer borophene and electron depletion for Cu(111), as shown in Fig. 3a,b, which supports the

**Table 1 | DFT calculated energies**

Boron sheets	$E$ (eV atom <sup>-1</sup> )	$\Delta E$ (meV atom <sup>-1</sup> )
Free-standing first layer	-6.333	-33
Free-standing second layer	-6.294	6
Free-standing bilayer	-6.355	-55
Free-standing $\beta_{12}$	-6.300	0

$E = \frac{E_{\text{tot}}}{n}$ , where  $E_{\text{tot}}$  is the total energy of one unit cell and  $n$  is the number of boron atoms in one unit cell.  $\Delta E = E_{\text{BS}} - E_{\beta_{12}}$ , where  $E_{\text{BS}}$  is the energy of different boron sheets and  $E_{\beta_{12}}$  is the energy of the free-standing  $\beta_{12}$  boron sheet.

**Table 2 | Charge transfer from Cu(111) to the different boron layers, and Ag(111) to the boron layer  $\beta_{12}$** 

Boron sheets	Average charge transfer (e atom <sup>-1</sup> )	$E_{\text{ads1}}$ (eV atom <sup>-1</sup> )	$E_{\text{ads2}}$ (eV Å <sup>-2</sup> )
First layer on Cu(111)	0.026	-0.41	-0.148
Bilayer on Cu(111)	0.012	-0.20	-0.143
$\beta_{12}$ on Ag(111)	0.014	-0.22	-0.074
Bilayer $\beta_{12}$ on Ag(111)	0.007	-0.12	-0.076

$E_{\text{ads1}} = [E_{\text{sys}} - (E_{\text{BS}} + E_{\text{sub}})]/n$ , where  $E_{\text{ads1}}$  is the average adsorption energy per boron atom,  $E_{\text{sys}}$  is the total energy of boron sheets on the Cu(111) and Ag(111) substrates,  $E_{\text{BS}}$  is the energy of different boron sheets,  $E_{\text{sub}}$  is the energy of Cu(111) and Ag(111) substrates, and  $n$  is the number of boron atoms.  $E_{\text{ads2}} = [E_{\text{sys}} - (E_{\text{BS}} + E_{\text{sub}})]/S$ , where  $E_{\text{ads2}}$  is the average adsorption energy per area and  $S$  is the area of boron sheets.

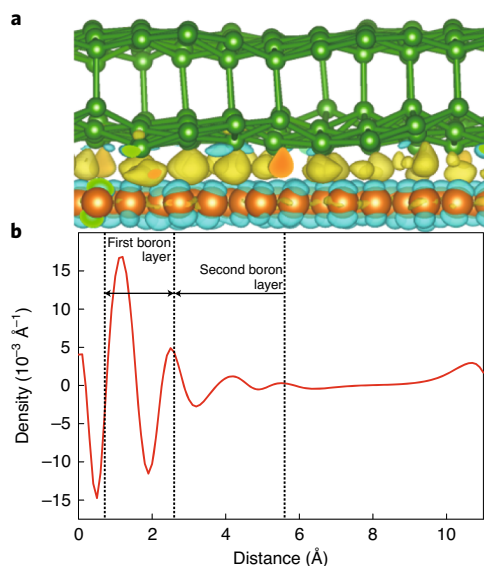


**Fig. 3 | Charge distribution between bilayer borophene and the Cu(111) substrate.** **a**, Isosurface plot of the charge redistribution between Cu planes (orange atoms) and relaxed borophene (green atoms). Electron depletion is shown in cyan and accumulation in yellow or orange. The isosurface is 0.007 e bohr<sup>-3</sup>. **b**, Planar-averaged electron density difference for bilayer borophene on Cu. The negative and positive areas indicate electron accumulation and depletion, respectively.

transfer of electrons to the first boron layer of bilayers borophene. The clearly positive and negative regions on the first boron layer suggest that the excess electrons are transferred from the first layer to the second boron layer, which results in the redistribution of the in-plane electrons in bilayer borophene, which is also beneficial for the growth of the bilayer boron sheet.

As discussed in more detail in Supplementary Fig. 1, the temperature window (600–750 K) for the formation of bilayer borophene is narrower than that for monolayer borophene (600–850 K), which suggests that the growth parameters for the formation of bilayer borophene are more complicated than those for monolayer borophene. Moreover, small boron clusters are formed on monolayer borophene prior to the formation of bilayer borophene (Supplementary Fig. 3). Therefore, we assume that the growth of bilayer boron is associated with the growth process and the high affinity of boron for the copper surface.

### Properties of bilayer borophene

We performed an ex situ X-ray photoelectron spectroscopy (XPS) characterization on both monolayer and bilayer borophene on Cu(111). The samples were prepared in ultrahigh vacuum chambers, then removed and transferred to another ultrahigh vacuum

chamber equipped with XPS. During the transfer the samples were exposed to ambient conditions. Figure 4a shows the XPS spectra of boron measured on a sample with almost a full covering of bilayer borophene on Cu(111). It is very interesting that the B 1s signal exhibited two peaks centred at 191.5 and 187.7 eV (Fig. 4a). The main component at 187.7 eV corresponds to a B–B bond according to the reported value obtained for bulk boron<sup>58</sup> and for borophene on metal surfaces<sup>14,15,36,59</sup>, whereas the peak with a higher binding energy at 191.5 eV corresponds to a B–O bond<sup>14,15,36</sup>. The extracted ratio of oxidized boron atoms is about 23%, which indicates that only a small portion of the boron atoms was oxidized after exposure to air. The oxidized boron atoms may also be due to a small amount of monolayer borophene on the measured area of the sample. However, for monolayer borophene on Cu(111), only the B–O peak was observed in the XPS spectra (Fig. 4b), which suggests that the monolayer borophene on Cu(111) was completely oxidized. The XPS data provide strong evidence for enhanced chemical stability and anti-oxidation of the bilayer borophene compared with those of the monolayer, which suggests that bilayer borophene may be a better candidate for device applications.

The calculated band structure and the corresponding decomposed orbital-resolved DOS of bilayer borophene are shown in Fig. 4c–e. Several bands cross the Fermi level indicated the metallicity of bilayer boron, and both the Cu-supported and free-standing bilayer borophene are metallic. The DOS of the bilayer borophene around the Fermi level were contributed mainly by the boron  $p$  orbitals, and more specifically the  $p_z$  orbital rather than the  $p_x$  and  $p_y$  orbitals. Moreover, the DOS contributed by the  $p_x$  and  $p_y$  orbitals of boron were mainly located at occupied states (Fig. 4e), and the  $p_z$  orbitals in unoccupied states contributed more quickly than those in the occupied states. According to the tunnelling mechanism of STM, the  $p_z$  orbital of the surface interacts with the STM tip more strongly than do the  $p_x$  and  $p_y$  orbitals. Therefore, the DOS in the occupied states detected by scanning tunnelling spectroscopy (Fig. 4f) should be suppressed, which leads to the unoccupied DOS increasing a little more quickly. Therefore, the distribution of the total DOS is in good agreement with the experimental  $dI/dV$  curves, which provides further support for our structural model of bilayer borophene. Additionally, the electronic structures of the free-standing first and second boron layers were calculated separately (Supplementary Fig. 18), and showed metallic behaviours for both structures.

Our findings suggest that boron atoms in bilayer borophene promote the transfer of electrons and balance the excess electrons to strengthen the stability of the bilayer system. Compared with the Ag(111) substrate, the Cu surface provides a better substrate for the

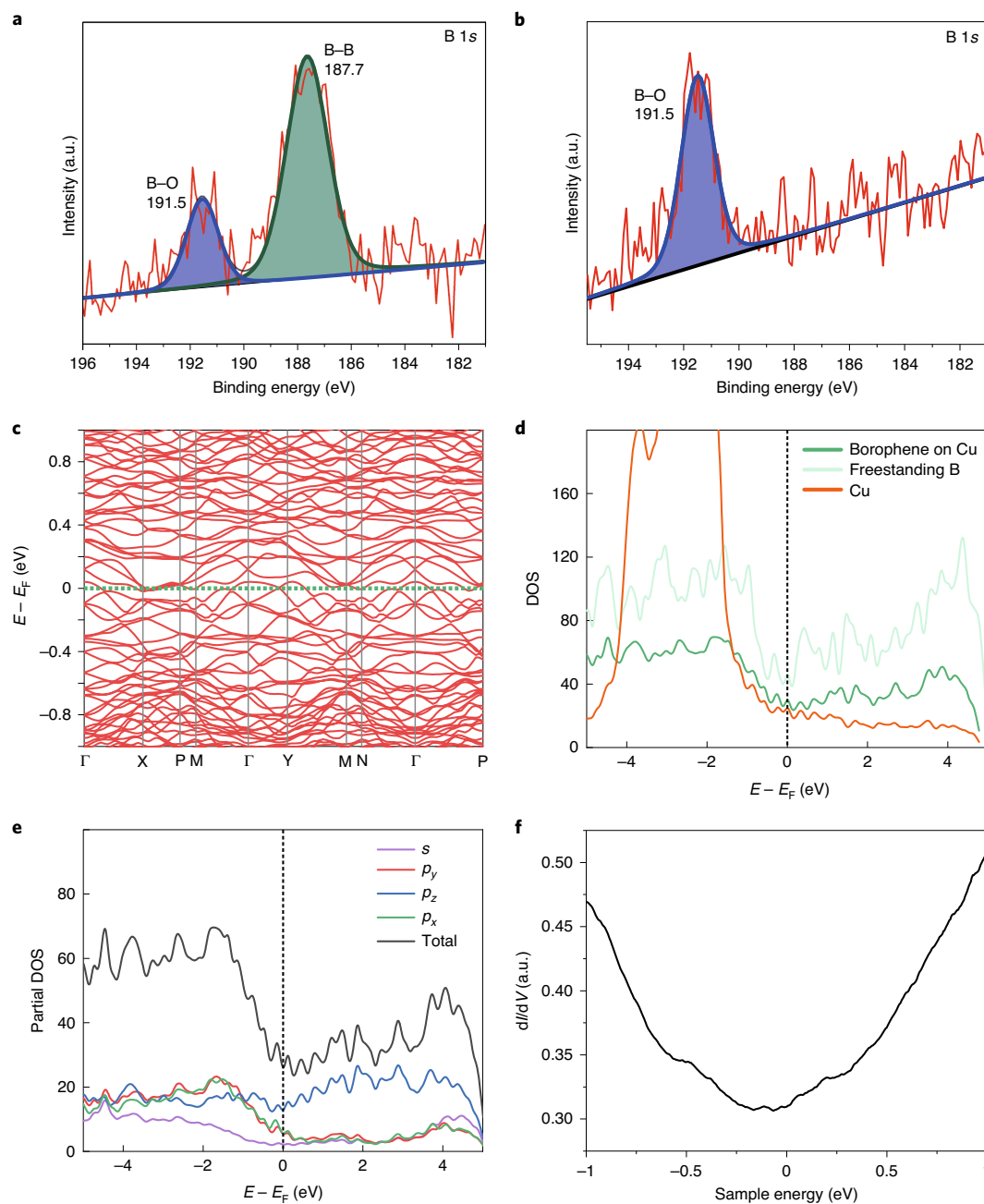


**Fig. 4 | The anti-oxidation ability and electronic structures of borophene on Cu(111).** **a,b**, The ex situ XPS spectra of bilayer borophene almost fully covering Cu(111) (**a**) and of monolayer borophene on Cu(111) (**b**) after exposure to air. The red, dark blue and dark green lines correspond to the original data, fitting lines and sum of fitting lines, respectively. The integral areas for B-O and B-B are shaded blue and light green, respectively. **c**, Calculated band structure of free-standing bilayer borophene. **d**, Calculated DOS for the relaxed borophene on Cu(111) (green line), for the same structure relaxed in vacuum (light green line) and for Cu (orange line). **e**, Partial DOS for the relaxed bilayer borophene on Cu(111). **f**, The experimental  $dI/dV$  spectra of bilayer borophene on Cu(111). a.u., arbitrary units.

formation of bilayer borophene. Although, experimentally, the Cu substrate appears to be the prerequisite for the formation of bilayer borophene, the energetic stability of bilayer borophene implies that it is sufficiently stable to enable its decoupling from the substrate for further studies and device fabrication. Moreover, bilayer boron is predicted to exhibit more flexibility than the monolayer form and to be able to withstand larger critical strains<sup>60</sup>. Certainly, it will be interesting to modulate the electronic and magnetic properties of the bilayer via the intercalation of transition metal atom guided by theoretical investigations<sup>61</sup>.

## Conclusion

In summary, large-scale, single-crystalline bilayer boron sheets were synthesized by epitaxial growth on the Cu(111) substrate. Combined experimental STM measurements and first-principles calculations show that a borophene bilayer consists of stacked layers of zigzag boron-chain structures. The first and second boron layers have vacancy concentrations of 5/36 and 1/6, respectively; interlayer covalent bonds between four-coordinated boron atoms are formed, which leads to a better thermal stability of the bilayer compared with that of the  $\beta_{12}$  monolayer. The larger adsorption energy of

monolayer boron on Cu(111) than that on Ag(111) and the greater electron transfer from Cu(111) to monolayer boron are probably the reasons for the growth of bilayer on monolayer borophene on Cu(111). The successful bottom-up synthesis of bilayer boron sheet provides opportunities and challenges for the characterization of their physical properties. The high quality of bilayer borophene on a metal surface and, in particular, its large size and single-crystalline nature may enable the fabrication of borophene-based devices, such as ultracapacitor, photonic and plasmonic devices, and electronic biomedical devices with a high sensitivity for signal transmission and detection.

### Online content

Any methods, additional references, Nature Research reporting summaries, source data, extended data, supplementary information, acknowledgements, peer review information; details of author contributions and competing interests; and statements of data and code availability are available at <https://doi.org/10.1038/s41557-021-00813-z>.

Received: 18 January 2021; Accepted: 16 September 2021;

Published online: 11 November 2021

### References

- Geim, A. K. & Novoselov, K. S. The rise of graphene. *Nat. Mater.* **6**, 183–191 (2007).
- Chen, L. et al. Spontaneous symmetry breaking and dynamic phase transition in monolayer silicene. *Phys. Rev. Lett.* **110**, 085504 (2013).
- Geim, A. K. & Grigorieva, I. V. Van der Waals heterostructures. *Nature* **499**, 419–425 (2013).
- Zhuo, Z., Wu, X. & Yang, J. Two-dimensional phosphorus porous polymorphs with tunable band gaps. *J. Am. Chem. Soc.* **138**, 7091–7098 (2016).
- Zhai, H. J. Hydrocarbon analogues of boron clusters—planarity, aromaticity and antiaromaticity. *Nat. Mater.* **2**, 827–833 (2003).
- Piazza, Z. A. et al. Planar hexagonal B<sub>36</sub> as a potential basis for extended single-atom layer boron sheets. *Nat. Commun.* **5**, 4113 (2014).
- Wang, L.-S. Photoelectron spectroscopy of size-selected boron clusters: from planar structures to borophenes and borospherenes. *Int. Rev. Phys. Chem.* **35**, 69–142 (2016).
- Tang, H. & Ismail-Beigi, S. Novel precursors for boron nanotubes: the competition of two-center and three-center bonding in boron sheets. *Phys. Rev. Lett.* **99**, 115501 (2007).
- Wu, X. et al. Two-dimensional boron monolayer sheets. *ACS Nano* **6**, 7443–7453 (2012).
- Penev, E. S., Bhowmick, S., Sadrzadeh, A. & Yakobson, B. I. Polymorphism of two-dimensional boron. *Nano Lett.* **12**, 2441–2445 (2012).
- Zhang, L. Z., Yan, Q. B., Du, S. X., Su, G. & Gao, H. J. Boron sheet adsorbed on metal surfaces: structures and electronic properties. *J. Phys. Chem. C* **116**, 18202–18206 (2012).
- Liu, H., Gao, J. & Zhao, J. From boron cluster to two-dimensional boron sheet on Cu(111) surface: growth mechanism and hole formation. *Sci. Rep.* **3**, 3238 (2013).
- Zhang, Z., Yang, Y., Gao, G. & Yakobson, B. I. Two-dimensional boron monolayers mediated by metal substrates. *Angew. Chem. Int. Ed.* **54**, 13022–13026 (2015).
- Mannix, A. J. et al. Synthesis of borophenes: anisotropic, two-dimensional boron polymorphs. *Science* **350**, 1513–1516 (2015).
- Feng, B. et al. Experimental realization of two-dimensional boron sheets. *Nat. Chem.* **8**, 563–568 (2016).
- Sheng, S. et al. Raman spectroscopy of two-dimensional borophene sheets. *ACS Nano* **13**, 4133–4139 (2019).
- Sun, X. et al. Two-dimensional boron crystals: structural stability, tunable properties, fabrications and applications. *Adv. Funct. Mater.* **27**, 1603300 (2017).
- Zhang, Z., Yang, Y., Penev, E. S. & Yakobson, B. I. Elasticity, flexibility, and ideal strength of borophenes. *Adv. Funct. Mater.* **27**, 1605059 (2017).
- Adamska, L., Sadasivam, S., Foley, J. J., Darancet, P. & Sharifzadeh, S. First-principles investigation of borophene as a monolayer transparent conductor. *J. Phys. Chem. C* **122**, 4037–4045 (2018).
- Huang, Y., Shirodkar, S. N. & Yakobson, B. I. Two-dimensional boron polymorphs for visible range plasmonics: a first-principles exploration. *J. Am. Chem. Soc.* **139**, 17181–17185 (2017).
- Lian, C. et al. Integrated plasmonics: broadband Dirac plasmons in borophene. *Phys. Rev. Lett.* **125**, 116802 (2020).
- Xiao, H. et al. Lattice thermal conductivity of borophene from first principle calculation. *Sci. Rep.* **7**, 45986 (2017).
- Li, D. et al. 2D boron sheets: structure, growth, and electronic and thermal transport properties. *Adv. Funct. Mater.* **8**, 1904349 (2019).
- Kong, L. et al. One-dimensional nearly free electron states in borophene. *Nanoscale* **11**, 15605–15611 (2019).
- Feng, B. et al. Dirac fermions in borophene. *Phys. Rev. Lett.* **118**, 096401 (2017).
- Feng, B. et al. Discovery of 2D anisotropic Dirac cones. *Adv. Mater.* **30**, 1704025 (2018).
- Penev, E. S., Kutana, A. & Yakobson, B. I. Can two-dimensional boron superconduct? *Nano Lett.* **16**, 2522–2526 (2016).
- Xiao, R. C. et al. Enhanced superconductivity by strain and carrier-doping in borophene: a first principles prediction. *Appl. Phys. Lett.* **109**, 122604 (2016).
- Cheng, C. et al. Suppressed superconductivity in substrate-supported β<sub>12</sub> borophene by tensile strain and electron doping. *2D Mater.* **4**, 025032 (2017).
- Zhong, Q. et al. Metastable phases of 2D boron sheets on Ag(111). *J. Phys. Condens. Mat.* **29**, 095002 (2017).
- Liu, X. et al. Geometric imaging of borophene polymorphs with functionalized probes. *Nat. Commun.* **10**, 1642 (2019).
- Zhong, Q. et al. Synthesis of borophene nanoribbons on Ag(110) surface. *Phys. Rev. Mater.* **1**, 021001 (2017).
- Wang, Y. et al. Realization of regular-mixed quasi-1D borophene chains with long-range order. *Adv. Mater.* **93**, e2005128 (2020).
- Li, W. et al. Experimental realization of honeycomb borophene. *Sci. Bull.* **63**, 282–286 (2018).
- Kiraly, B. et al. Borophene synthesis on Au(111). *ACS Nano* **13**, 3816–3822 (2019).
- Wu, R. et al. Large-area single-crystal sheets of borophene on Cu(111) surfaces. *Nat. Nanotechnol.* **14**, 44–49 (2019).
- Wu, R., Gozar, A. & Božović, I. Large-area borophene sheets on sacrificial Cu(111) films promoted by recrystallization from subsurface boron. *npj Quantum Mater.* **4**, 40 (2019).
- Vinogradov, N. A., Lyalin, A., Taketsugu, T., Vinogradov, A. S. & Preobrajenski, A. Single-phase borophene on Ir(111): formation, structure, and decoupling from the support. *ACS Nano* **13**, 14511–14518 (2019).
- Li, H. et al. Scalable production of few-layer boron sheets by liquid-phase exfoliation and their superior supercapacitive performance. *ACS Nano* **12**, 1262–1272 (2018).
- Ranjan, P. et al. Freestanding borophene and its hybrids. *Adv. Mater.* **31**, e1900353 (2019).
- Ranjan, P., Lee, J. M., Kumar, P. & Vinu, A. Borophene: new sensation in flatland. *Adv. Mater.* **32**, e2000531 (2020).
- Cao, Y. et al. Correlated insulator behaviour at half-filling in magic-angle graphene superlattices. *Nature* **556**, 80–84 (2018).
- Cao, Y. et al. Unconventional superconductivity in magic-angle graphene superlattices. *Nature* **556**, 43–50 (2018).
- Wu, Z. et al. Even-odd layer-dependent magnetotransport of high-mobility Q-valley electrons in transition metal disulfides. *Nat. Commun.* **7**, 12955 (2016).
- de la Barrera, S. C. et al. Tuning Ising superconductivity with layer and spin-orbit coupling in two-dimensional transition-metal dichalcogenides. *Nat. Commun.* **9**, 1427 (2018).
- Kumar, P. et al. Laser shock tuning dynamic interlayer coupling in graphene-boron nitride moiré superlattices. *Nano Lett.* **19**, 283–291 (2018).
- Cui, J. et al. Transport evidence of asymmetric spin-orbit coupling in few-layer superconducting 1T<sub>r</sub>-MoTe<sub>2</sub>. *Nat. Commun.* **10**, 2044 (2019).
- Moriya, R. et al. Emergence of orbital angular moment at van Hove singularity in graphene/h-BN moiré superlattice. *Nat. Commun.* **11**, 5380 (2020).
- Gao, N., Wu, X., Jiang, X., Bai, Y. & Zhao, J. Structure and stability of bilayer borophene: the roles of hexagonal holes and interlayer bonding. *FlatChem* **7**, 48–54 (2018).
- Nakhaee, M., Ketabi, S. A. & Peeters, F. M. Dirac nodal line in bilayer borophene: tight-binding model and low-energy effective Hamiltonian. *Phys. Rev. B* **98**, 115413 (2018).
- Li, D. et al. From two- to three-dimensional van der Waals layered structures of boron crystals: an ab initio study. *ACS Omega* **4**, 8015–8021 (2019).
- Xu, S. G., Zheng, B., Xu, H. & Yang, X. B. Ideal nodal line semimetal in a two-dimensional boron bilayer. *J. Phys. Chem. C* **123**, 4977–4983 (2019).
- Zhao, Y., Zeng, S. & Ni, J. Superconductivity in two-dimensional boron allotropes. *Phys. Rev. B* **93**, 014502 (2016).
- Banerjee, S., Periyasamy, G. & Pati, S. K. Possible application of 2D-boron sheets as anode material in lithium ion battery: a DFT and AIMD study. *J. Mater. Chem. A* **2**, 3856 (2014).
- Chen, W. J. et al. B<sub>48</sub><sup>-</sup>: a bilayer boron cluster. *Nanoscale* **13**, 3868–3876 (2021).
- Liu, X. et al. Borophene synthesis beyond the single-atomic-layer limit. *Nat. Mater.* <https://doi.org/10.1038/s41563-021-01084-2> (2021).

57. Zhang, C. et al. Interlayer couplings, moiré patterns, and 2D electronic superlattices in MoS<sub>2</sub>/WSe<sub>2</sub> hetero-bilayers. *Sci. Adv.* **3**, e1601459 (2017).
58. Ong, C. W. et al. X-ray photoemission spectroscopy of nonmetallic materials: electronic structures of boron and B<sub>2</sub>O<sub>3</sub>. *J. Appl. Phys.* **95**, 3527–3534 (2004).
59. Guoan Tai, T. H. et al. Synthesis of atomically thin boron films on copper foils. *Angew. Chem. Int. Ed.* **54**, 15473–15477 (2015).
60. Zhong, H., Huang, K., Yu, G. & Yuan, S. Electronic and mechanical properties of few-layer borophene. *Phys. Rev. B* **98**, 054104 (2018).
61. Zhang, X., Sun, Y., Ma, L., Zhao, X. & Yao, X. Modulating the electronic and magnetic properties of bilayer borophene via transition metal atoms intercalation: from metal to half metal and semiconductor. *Nanotechnology* **29**, 305706 (2018).

**Publisher's note** Springer Nature remains neutral with regard to jurisdictional claims in published maps and institutional affiliations.

© The Author(s), under exclusive licence to Springer Nature Limited 2021

## Methods

**Experiments.** The experiments were performed in our homebuilt ultrahigh vacuum MBE–STM system, with a base pressure of approximately  $5.8 \times 10^{-11}$  torr for the STM chamber, whereas it was  $\sim 2.9 \times 10^{-10}$  torr for the MBE chamber. The clean Cu(111) substrate was prepared by repeated cycles of Ar<sup>+</sup> ion sputtering and postannealing at 900 K. Pure boron (99.9999%) was evaporated by a commercial electron-beam evaporator onto the clean Cu(111) substrate. During boron growth, the Cu(111) substrate was kept at appropriate temperatures and the pressure was greater than  $5.0 \times 10^{-10}$  torr. After growth, the sample was transferred to the STM chamber without breaking the vacuum, and the STM and scanning tunnelling spectroscopy measurements were all obtained under 77 K with a chemically etched tungsten tip. The XPS spectra were conducted ex situ by taking the prepared sample out in air and transferring it into an XPS system with a resolution of 0.48 eV (ThermoFisher Scientific ESCALAB 250X with a monochromatic Al K $\alpha$  X-ray source,  $h\nu = 1,486.6$  eV). The binding energy and Fermi level were calibrated by measurements on pure Ag ( $3d_{5/2}$ , 368.2 eV) and Cu ( $2p_{3/2}$ , 932.6 eV) surfaces. The diameter of the surface area in the XPS measurements was about 300  $\mu\text{m}$ , and XPSPEAK software was used for the data fitting. The XPS peaks were fitted with a mixture of Gaussian and Lorentzian functions (20% Lorentzian). The full-width at half-maximum of the B–B peaks was 1.8, and the full-width at half-maximum for the B–O peak was 1.4. The peak with a maximum at 187.7 eV (attributed to B–B bonds) had a greater full-width at half-maximum, which indicate that the two layers of B–B bonds have slightly different chemical environment.

**Calculations.** First-principles calculations were performed based on ab initio DFT using the VASP 5.4.4 program<sup>62</sup>. The generalized gradient approximation and Perdew–Burke–Ernzerhof exchange–correlation functional were adopted<sup>63–65</sup>. Grimme D3 correction was used to describe the interlayer van der Waals interactions<sup>66</sup>. A well-converged plane-wave cutoff of 400 eV was used and the atomic coordinates were allowed to relax until the forces on the ions were less than  $0.03 \text{ eV } \text{\AA}^{-1}$ . The electronic convergence criterion was set to  $1 \times 10^{-5}$  eV. The reduced Brillouin zone was sampled with a  $\Gamma$ -centred  $2 \times 1 \times 1$  k-point mesh for optimization and a  $4 \times 2 \times 1$  k-point mesh for static and electronic structure calculations<sup>67,68</sup>. A 15  $\text{\AA}$  vacuum space was used in all the calculations. We calculated the charge transfer based on a Bader analysis<sup>69,70</sup>. To simulate the STM images, a system with a bilayer boron sheet on a one-layer fixed Cu(111) substrate was adopted, which included 88 Cu atoms and 366 B atoms. The simulated STM image was constructed on the basis of Tersoff–Hamann theory and was visualized using the p4VASP program with the constant current mode<sup>71</sup>. The  $\beta_{12}$  monolayer on the Ag(111) model was constructed using a  $\sqrt{3} \times 1$  supercell of Ag(111) and one unit cell of the  $\beta_{12}$  monolayer. The lattice mismatch between  $\beta_{12}$  and Ag(111) was no more than 1.5% (Ag(111), 2.90 and 5.00  $\text{\AA}$ ;  $\beta_{12}$ , 2.92 and 5.07  $\text{\AA}$ ). The model for a bilayer boron sheet on Cu(111) was constructed using a  $\sqrt{178} \times \sqrt{39}$  supercell of Cu(111) and one unit cell of the bilayer boron. The lattice mismatch between the bilayer borophene and the Cu substrate was smaller than 0.3% (Cu(111),  $a = 16.2$   $\text{\AA}$ ,  $b = 34.0$   $\text{\AA}$  and  $\theta = 68.5^\circ$ ; bilayer boron,  $a = 16.1$   $\text{\AA}$ ,  $b = 34.2$   $\text{\AA}$ , and  $\theta = 69.2^\circ$ ). The k-mesh for the  $\beta_{12}$  unit cell and bilayer boron was  $16 \times 8 \times 1$  and  $2 \times 1 \times 1$  for the reduced Brillouin zone.

## Data availability

Data that support the finding of this study are available within the article and its Supplementary Information and data files. Data for the Supplementary figures and DFT-calculated structures are provided as Supplementary Data files. Source data are provided with this paper.

## References

- Kresse, G. F. Efficient iterative schemes for ab initio total-energy calculations using a plane-wave basis set. *Phys. Rev. B* **54**, 11169 (1996).
- Bloch, P. E. Projector augmented-wave method. *Phys. Rev. B* **50**, 17953 (1994).
- Perdew, J. P. et al. Generalized gradient approximation made simple. *Phys. Rev. Lett.* **77**, 3865 (1996).
- Kresse, G. & Joubert, D. From ultrasoft pseudopotentials to the projector augmented-wave method. *Phys. Rev. B* **59**, 1758 (1999).
- Grimme, S., Antony, J., Ehrlich, S. & Krieg, H. A consistent and accurate ab initio parametrization of density functional dispersion correction (DFT-D) for the 94 elements H–Pu. *J. Chem. Phys.* **132**, 154104 (2010).
- Methfessel, M. & Paxton, A. T. High-precision sampling for Brillouin-zone integration in metals. *Phys. Rev. B* **40**, 3616–3621 (1989).
- Monkhorst, H. J. & Pack, J. D. Special points for Brillouin-zone integrations. *Phys. Rev. B* **13**, 5188–5192 (1976).
- Bader, R. F. W. *Atoms in Molecules: A Quantum Theory* (Oxford Univ. Press, 1990).
- Henkelman, G., Arnaldsson, A. & Jónsson, H. A fast and robust algorithm for Bader decomposition of charge density. *Comp. Mater. Sci.* **36**, 354–360 (2006).
- Tersoff, J. & Hamann, D. R. Theory of the scanning tunneling microscope. *Phys. Rev. B* **31**, 805–813 (1985).

## Acknowledgements

This work was financially supported by the National Key R&D Program of China (2018YFE0202700, 2016YFA0200602, 2016YFA0300904 and 2016YFA0202301), the National Natural Science Foundation of China (12134019, 22073087, 11825405, 21573204 and 21890751), the Beijing Natural Science Foundation (Z1800007), the Strategic Priority Research Program of the Chinese Academy of Sciences (XDB30000000 and XDB01020300), the Anhui Initiative in Quantum Information Technologies (AHY090400), the National Program for Support of Top-notch Young Professional, NSFC-MAECI (51861135202) and the Super Computer Centre of USTCSCC and SCCAS.

## Author contributions

L.C. and K.W. designed and conceived this research. C.C., W.L., X.W., P.Z., C.M. and Y.W. performed the experiments under the supervision of L.C. and K.W. H.L. and Z.Z. did the calculation works under the supervision of X.W. B.F. and P.C. participated in the data analysis and discussion. All the authors contributed to the writing of the manuscript.

## Competing interests

The authors declare no competing interests.

## Additional information

**Supplementary information** The online version contains supplementary material available at <https://doi.org/10.1038/s41557-021-00813-z>.

**Correspondence and requests for materials** should be addressed to Xiaojun Wu, Kehui Wu or Lan Chen.

**Peer review information** *Nature Chemistry* thanks Prashant Kumar and the other, anonymous, reviewer(s) for their contribution to the peer review of this work.

**Reprints and permissions information** is available at [www.nature.com/reprints](http://www.nature.com/reprints).